

Journal of Materials Chemistry A

Accepted Manuscript



This is an *Accepted Manuscript*, which has been through the Royal Society of Chemistry peer review process and has been accepted for publication.

Accepted Manuscripts are published online shortly after acceptance, before technical editing, formatting and proof reading. Using this free service, authors can make their results available to the community, in citable form, before we publish the edited article. We will replace this *Accepted Manuscript* with the edited and formatted *Advance Article* as soon as it is available.

You can find more information about *Accepted Manuscripts* in the [Information for Authors](#).

Please note that technical editing may introduce minor changes to the text and/or graphics, which may alter content. The journal's standard [Terms & Conditions](#) and the [Ethical guidelines](#) still apply. In no event shall the Royal Society of Chemistry be held responsible for any errors or omissions in this *Accepted Manuscript* or any consequences arising from the use of any information it contains.

ARTICLE

Transformative route to nanoporous manganese oxides of controlled oxidation states with identical textural properties

Cite this: DOI: 10.1039/x0xx00000x

Received 00th January 2012,
Accepted 00th January 2012

DOI: 10.1039/x0xx00000x

www.rsc.org/Jae Hwa Lee,^{a,‡} Young Jin Sa,^{a,‡} Tae Kyung Kim,^a Hoi Ri Moon*^a and Sang Hoon Joo*^b

Nanoporous nanocrystalline metal oxides with tunable oxidation states are crucial for controlling their catalytic, electronic, and optical properties. However, previous approaches to modulating oxidation states in nanoporous metal oxides commonly lead to the breakdown of nanoporous structure as well as involve concomitant changes in their morphology, pore size, surface area, and nanocrystalline size. Herein, we present a transformative route to nanoporous metal oxides with various oxidation states using manganese oxides as examples. Thermal conversion of Mn-based metal–organic frameworks (Mn–MOFs) under controlled temperature and atmosphere yielded a series of nanoporous manganese oxides with continuously tuned oxidation states: MnO, Mn₃O₄, Mn₅O₈, and Mn₂O₃. This transformation enabled the preparation of low-oxidation phase MnO and metastable intermediate phase Mn₅O₈ with nanoporous architectures, which were previously rarely accessible. Significantly, nanoporous MnO, Mn₃O₄, and Mn₅O₈ had very similar morphology, surface area, and crystalline size. We investigated electrocatalytic activity of nanoporous manganese oxides for the oxygen reduction reaction (ORR) to identify the role of oxidation states, and observed oxidation state-dependent activity and kinetics for the ORR.

1. Introduction

Nanoporous metal oxide materials with crystalline frameworks have been of prime importance in various fields, including adsorption, catalysis, and energy conversion and storage.^{1–5} In these materials, the control of oxidation states is crucial for tailoring their catalytic, electronic, and optical properties. During the last two decades, diverse soft and hard templating strategies have been developed to prepare nanoporous metal oxides with a rich variety of compositions and structures.^{6–14} However, these methods usually involve solution processes and subsequent high-temperature annealing steps, which have limited the range of stable metal oxide phases predominantly to those with high oxidation numbers. In addition, post-synthetic thermal treatments aimed for changing the oxidation states of nanoporous metal oxides often result in the growth of nanocrystalline domain size, which consequently leads to the breakdown of the nanoporous structure. Hence, the preparation of nanoporous metal oxides with broadly tunable oxidation states, particularly those with low oxidation or metastable intermediate phases, has been challenging.

Recently, *conversion reactions* that transform pre-synthesized nanoscale or microscale inorganic solid *precursors* into new materials have emerged as new synthetic toolboxes in materials chemistry.^{15–19} Conversion reactions have been explored extensively with various types of precursors, and have enabled the synthesis of new materials with a high degree of compositional and structural complexity. The versatility of conversion reactions can be exemplified in the preparation of thermodynamically unfavorable hollow nanoparticles from solid analogues by exploiting the nanoscale Kirkendall effect²⁰ or galvanic replacement reaction.²¹ In the context of conversion reactions, metal–organic frameworks (MOFs), in which inorganic and organic building blocks are alternatively arranged in a periodic manner, can serve as excellent precursors, and accordingly, conversion reactions utilizing MOFs are currently being actively pursued.^{22–31} In this line of efforts, we recently reported the preparation of nanoporous non-siliceous metal oxides with nanocrystalline frameworks via thermal conversion of MOFs for the first time.³⁰

Herein, we demonstrate that conversion reactions using MOFs as precursors can be successfully exploited to prepare

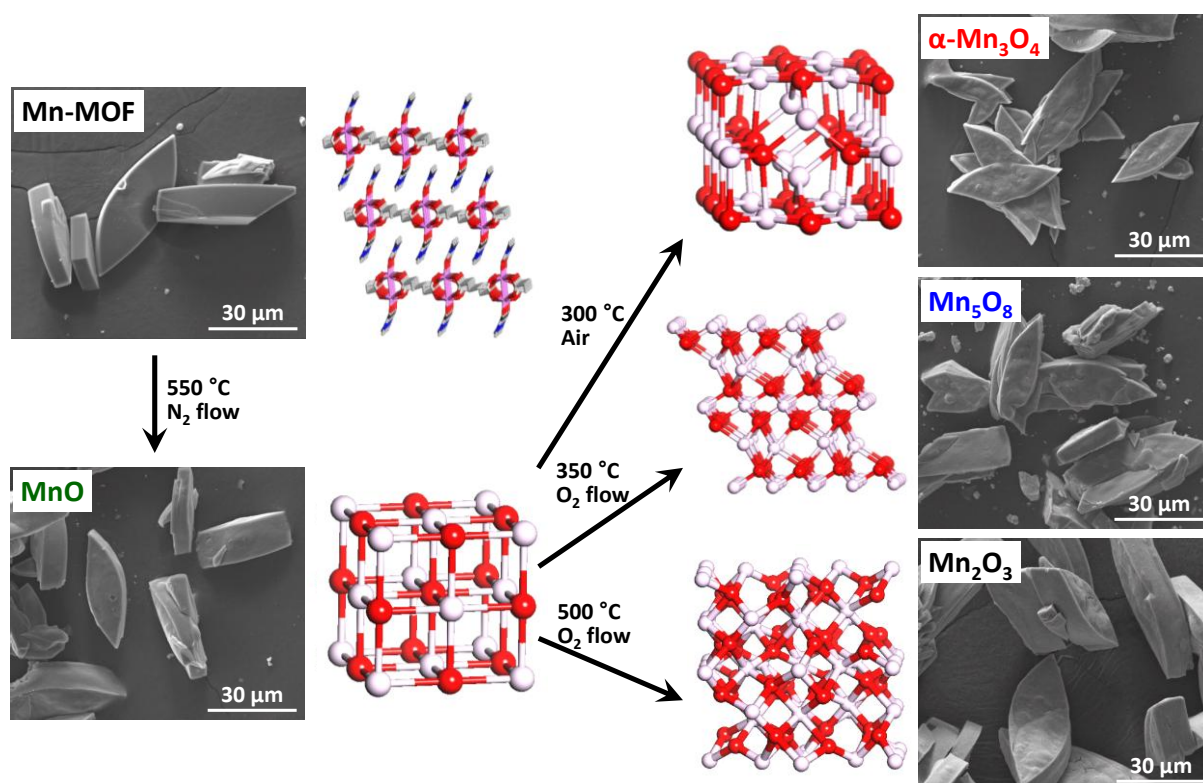


Fig. 1 SEM images and atomic structures of Mn-MOF and converted manganese oxides during structural transformation of Mn-MOF into MnO, Mn₃O₄, Mn₅O₈ and Mn₂O₃.

nanoporous nanocrystalline metal oxides with tunable oxidation states. Manganese oxides were chosen as a model system because they can exist in various oxidation states³² and are the centers of great interests in energy conversion and storage as well as catalysis.³³⁻³⁶ We show that sequential conversion reactions are capable of transforming a Mn-based MOF (Mn-MOF) into nanoporous nanocrystalline manganese oxides with continuously tuned oxidation states, MnO, Mn₃O₄, Mn₅O₈, and Mn₂O₃, with conservation of the original morphology of the Mn-MOF crystals (Fig. 1). Importantly, these conversion reactions enabled the preparation of low-oxidation-state MnO and metastable intermediate Mn₅O₈ phases with nanoporous nanocrystalline architecture, which was previously difficult to access. Nanoporous MnO, Mn₃O₄, and Mn₅O₈ have almost identical textural properties, including their morphology, surface areas, pore volumes, and size of nanocrystals composing nanoporous frameworks. The textural similarity among the series of manganese oxides allowed them to be used as a system for studying the oxidation-state effect in catalysis; previous works related to such effect were mostly performed with a series of catalysts possessing various other variables that can affect catalytic performances.³⁷⁻⁴⁰ We investigated the electrocatalytic activity of these nanoporous manganese oxides for the oxygen reduction reaction (ORR), and observed oxidation-state-dependent catalytic activity and kinetics in the ORR.

2. Experimental Section

2.1 Materials

All chemicals and solvents were of reagent grade and used without further purification. *Meso*-butane-1,2,3,4-tetracarboxylic acid (H₄BuTC, >98%), and *N,N*-dimethylacetamide (DMA, >99%) were supplied by TCI. Mn(NO₃)₂·4H₂O (>97%) was purchased from Aldrich.

2.2 Synthesis of Mn-MOF ([Mn₂(BuTC)(DMA)₂]_{*n*})

H₄BuTC (0.037 g, 0.16 mmol) was dissolved in DMA (2.5 mL), and mixed with a DMA (2.5 mL) solution of Mn(NO₃)₂·4H₂O (0.080 g, 0.32 mmol). The solution was sealed in a glass jar, heated to 100 °C for 24 h, and then cooled to room temperature. Yellowish leaf-shaped crystals formed, which were filtered and washed briefly with the mother liquor. Yield: 35%. FT-IR (Nujol mull): ν_{C=O}(DMA), 1652 (s); ν_{O-C=O}, 1615, 1418 (s) cm⁻¹. Anal. Calcd for Mn₂C₁₆H₂₄O₁₀N₂: C, 37.37; H, 4.70; N, 5.45. Found: C, 37.53; H, 4.59; N, 5.44.

2.3 Conversion reactions of Mn-MOF into manganese oxides

MnO: Solid Mn-MOF was heated at 5 °C min⁻¹ under a nitrogen flow of 60 mL min⁻¹. After reaching the target temperature of 550 °C, the material was maintained at that

temperature for 12 h. After cooling to room temperature, black solid was obtained.

Mn_3O_4 : As-synthesized MnO solid was heated in a box furnace (ambient air environment) at $5\text{ }^\circ\text{C min}^{-1}$. After reaching the target temperature of $300\text{ }^\circ\text{C}$, the material was maintained at that temperature for 2 h. After cooling to room temperature, brownish solid was obtained.

Mn_5O_8 : As-synthesized MnO solid was heated at $1\text{ }^\circ\text{C min}^{-1}$ under an oxygen flow of 100 mL min^{-1} . After reaching the target temperature of $350\text{ }^\circ\text{C}$, the material was maintained at that temperature for 2 h. After cooling to room temperature, blackish solid was obtained.

Mn_2O_3 : As-synthesized MnO was heated at $1\text{ }^\circ\text{C min}^{-1}$ under an oxygen flow of 100 mL min^{-1} . After reaching the target temperature of $500\text{ }^\circ\text{C}$, the material was maintained at that temperature for 2 h. After cooling to room temperature, dark grey powder was obtained.

2.4. Single-crystal X-ray crystallography

A single-crystal of Mn-MOF was coated with paratone-*N* oil, and the diffraction data were measured at 100 K with synchrotron radiation ($\lambda = 0.69999\text{ \AA}$) on an ADSC Quantum-210 detector at 2D SMC with a silicon (111) double crystal monochromator (DCM) at the Pohang Accelerator Laboratory, Republic of Korea. The ADSC Q210 ADX program⁴¹ was used for data collection, and HKL3000sm (Ver. 703r)⁴² was used for cell refinement, reduction, and absorption correction. The crystal structures were solved by direct methods and refined by full-matrix least-squares calculations with the SHELX-97 computer program.⁴³ The positions of all non-hydrogen atoms were refined with anisotropic displacement factors. The hydrogen atoms were positioned geometrically using a riding model.

2.5 Characterization methods

All characterizations were carried out at the Ulsan National Institute of Science and Technology (UNIST) Central Research Facilities (UCRF) Center. Infrared spectra were recorded with a ThermoFisher Scientific iS10 FT-IR spectrometer. Elemental analyses (for C, H, N, S, and O) were performed by using a Thermo Scientific Flash 2000 series CHNS/O analyzer. Thermogravimetric analyses (TGA) were performed under nitrogen gas at a scan rate of $5\text{ }^\circ\text{C min}^{-1}$, using a TGA Q50 from TA Instruments. X-ray photoelectron spectroscopy (XPS) was performed on a K-alpha from Thermo Fisher. X-ray powder diffraction (XRPD) data were recorded on a Bruker D8 advance diffractometer at 40 kV and 40 mA and a Bruker D2 phaser diffractometer at 30 kV and 10 mA for Cu K α ($\lambda = 1.541\text{ \AA}$), with a step size of 0.02° in 2θ . Scanning electron microscope (SEM) images were taken using a Quanta 200 microscope (FEI) operating at 18 kV. Transmission electron microscope (TEM) images and energy dispersive X-ray spectra were obtained with a JEOL JEM-2100F microscope. The nitrogen adsorption-desorption isotherms were measured at 77 K using liquid nitrogen on a BELSORP-MAX. Prior to the adsorption measurement, the

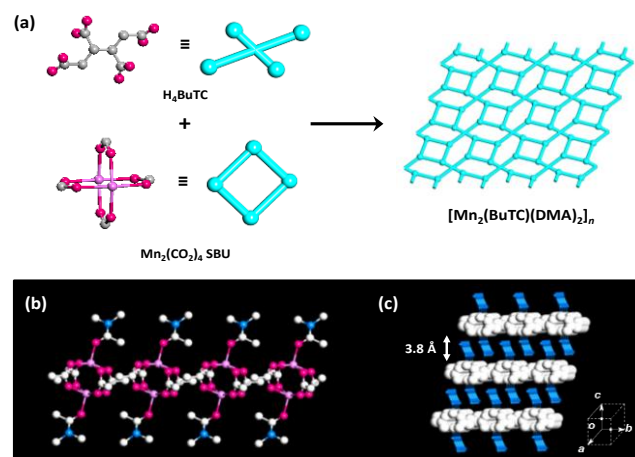


Fig. 2 Synthesis and single-crystal X-ray structure of Mn-MOF. (a) Synthetic scheme of Mn-MOF. (b) Side view of one layer of Mn-MOF. Hydrogen atoms and guest molecules are omitted for clarity (color scheme: C, white; O, purple; N, light blue; Mn, pink). (c) Entire structure of Mn-MOF (color scheme: 2-D layer, white; coordinating DMA, blue)

samples were evacuated at $200\text{ }^\circ\text{C}$ under vacuum ($p < 10^{-5}$ mbar) overnight. The specific surface area was determined in the relative pressure range from 0.05 to 0.3 of the Brunauer–Emmett–Teller (BET) plot, and the total pore volume was calculated from the amount adsorbed at a relative pressure of about 0.98–0.99. Pore size distribution curves were obtained from the corresponding isotherms using the Barrett–Joyner–Halenda (BJH) method.

2.6 Electrochemical measurements

Electrochemical characterization of the samples was carried out using an IviumStat electrochemical analyzer. The electrochemical experiments were performed at room temperature ($25\text{ }^\circ\text{C}$) and under atmospheric pressure using a three-compartment electrochemical cell. A graphite counter electrode and Hg/HgO reference electrode (XR400, Radiometer Analytical) with 1 M KOH (99.999%, Aldrich) filling solution were used. The Hg/HgO reference electrode was calibrated with respect to the reversible hydrogen electrode (RHE) before use. For this purpose, Pt wires were used as both the working electrode and counter electrode, and the potential cycle between -0.93 V and -0.87 V (vs. Hg/HgO) was applied with a scan rate of 1 mV s^{-1} in H_2 -saturated 0.1 M KOH solution. The resulting potential–current (V – I) curve after averaging the anodic and cathodic currents gave a result of $E(\text{RHE}) = E(\text{Hg}/\text{HgO}) + 0.887\text{ V}$. All potentials in this report were reported in the RHE scale.

For ORR performance measurement, a rotating ring disk electrode (RRDE) with a glassy carbon disk (GC, 4 mm in diameter) and a Pt ring (5 mm in inner diameter and 7 mm in outer diameter) was used as a working electrode (ALS, Cat. No. 012613). The RRDE was polished with 1.0 and $0.3\text{ }\mu\text{m}$ alumina suspensions to generate a mirror finish. For preparation of a catalyst ink, Nafion (5 wt% in isopropyl alcohol (IPA), Aldrich) was neutralized by 0.1 M NaOH

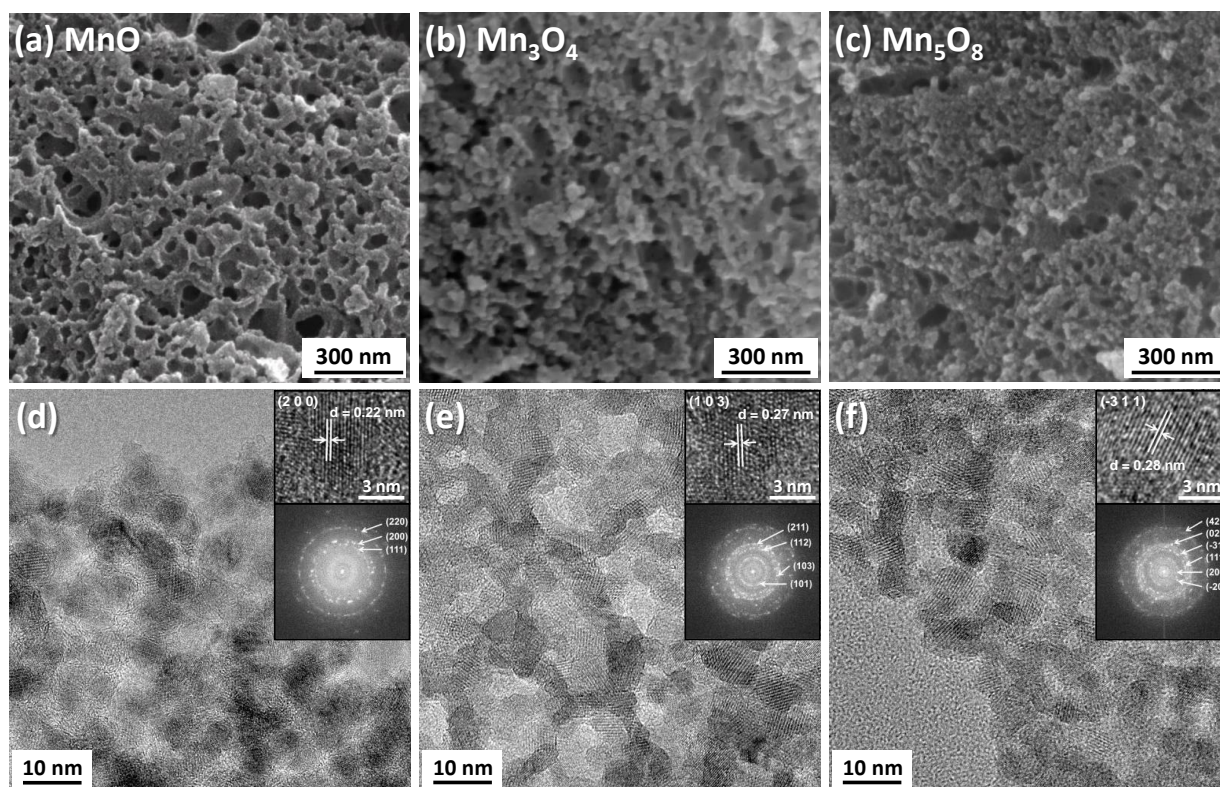


Fig. 3 Characterizations of converted manganese oxides. (a–c) SEM images, (d–f) TEM images, and (d–f, insets) HRTEM images and electron diffraction patterns of nanoporous MnO (a,d), Mn₃O₄ (b,e), and Mn₅O₈ (c,f).

(99.99%, Aldrich) at a volume ratio of Nafion : 0.1 M NaOH = 2 : 1 in order to prevent oxide passivation.⁴⁴ Commercial carbon black (Vulcan XC-72R) was added to the catalyst ink to overcome the low electrical conductivity of oxides. The catalyst ink was prepared by mixing 5 mg of catalyst, 12 mg of Vulcan, 116 μL of neutralized Nafion, 100 μL of deionized water, and 0.98 mL of IPA (>99.9%, Aldrich) with ultrasonication for at least 30 min. 3 μL of the catalyst ink was deposited onto the GC electrode with a micro-syringe. The resulting catalyst loading was 0.1 $\text{mg}_{\text{oxide}} \text{cm}^{-2}$. Prior to the electrochemical measurements, a potential cycle from 0.7 to 1.0 V was applied in a N₂-saturated 0.1 M KOH for 50 cycles at a scan rate of 100 mV s^{-1} for electrochemical cleaning. Subsequently, the cyclic voltammogram was obtained under the same condition used for electrochemical cleaning, except for the change in the scan rate of 20 mV s^{-1} for 3 cycles. Linear sweep voltammetry (LSV) curves for the ORR were obtained by cycling the potential from 1.1 to 0.2 V in an O₂-saturated 0.1 M KOH solution with O₂ purging at different rotating speeds. The anodic and cathodic sweeps for the ORR were averaged in order to correct the capacitive-current contribution.⁴⁴ The ORR measurement was independently repeated three times, and the averaged currents were used.

For the evaluation of four-electron selectivity, the potential of the Pt ring was fixed at 1.3 V (vs. RHE) during LSV scans for the ORR. The number of electrons transferred was calculated by the following equation:

$$n = \frac{4}{1 + \frac{I_R}{N \times I_D}}$$

Here, I_D , I_R , and N are the disk current, the ring current and the collection coefficient, respectively. The value of N was measured in 1 M KNO₃ + 2 mM K₃Fe(CN)₆ at a rotating speed of 1000 rpm, and was determined to be 0.47.

The four-electron selectivity was also assessed by Koutecký-Levich equation:

$$\frac{1}{I} = \frac{1}{I_K} + \frac{1}{I_L} = \frac{1}{I_K} - \frac{1}{0.62nFAD_0^{2/3} \nu^{-1/6} C_O \omega^{1/2}}$$

Here, I , I_L and I_K are the measured current, the diffusion-limited current and the kinetic current, respectively. F is the Faraday constant. ($9.65 \times 10^7 \text{ mA s mol}^{-1}$), A is the GC disk area. (0.126 cm^2), D_0 is the diffusion coefficient of O₂ in 0.1 M KOH solution ($1.9 \times 10^{-5} \text{ cm}^2 \text{ s}^{-1}$), ν is the kinematic viscosity of 0.1 M KOH. ($0.01 \text{ cm}^2 \text{ s}^{-1}$), C_O is the concentration of O₂ in 0.1 M KOH. ($1.2 \times 10^{-6} \text{ mol cm}^{-3}$), and ω is the rotation speed of the unit in radian per second.⁴⁵⁻⁴⁷

Before electrochemical impedance spectroscopy (EIS) measurement, the potential was cycled from 0.7 to 1.0 V for 50 cycles in N₂-saturated 0.1 M KOH solution. Then, impedance spectra were obtained in O₂-saturated 0.1 M KOH at the fixed potential of 0.7 V (vs. RHE) in the frequency range varying from 10 kHz to 0.05 Hz.

3. Results and discussion

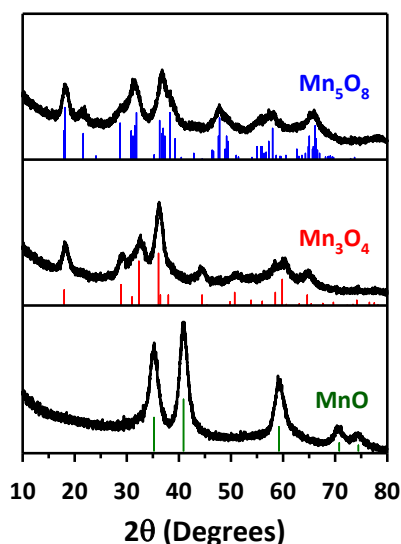


Fig. 4 XRPD patterns of converted manganese oxides.

3.1. Synthesis of Mn-MOF precursor

We began with the synthesis of the Mn-MOF precursor. A solvothermal reaction of $\text{Mn}(\text{NO}_3)_2 \cdot 4\text{H}_2\text{O}$ and aliphatic ligand, *meso*-butane-1,2,3,4-tetracarboxylic acid (H_4BuTC), in *N,N*-dimethylacetamide (DMA) solvent at 100 °C for 24 h afforded yellowish leaf-shaped crystals of $[\text{Mn}_2(\text{BuTC})(\text{DMA})_2]_n$ (Fig. 1 and 2). Single-crystal X-ray crystallographic data⁴⁸ (Fig. 2 and S1† and Tables S1† and S2†) revealed that Mn-MOF is constructed with $\text{Mn}_2(\text{COO})_4$ paddle-wheel clusters as secondary building units interconnected by BuTC ligand to form a 2-dimensional layer. In the Mn-MOF, each Mn^{II} ion is coordinated with four oxygen atoms of four different BuTC ligands in the equatorial positions and an oxygen atom of a DMA molecule at the axial position to show a square-pyramidal coordination geometry. Four carboxylate groups of four different BuTC ligands bridge between the two Mn^{II} centers in a *syn-syn* bidentate mode, forming a paddle-wheel shaped SBU. The Mn-Mn distance in a SBU is 3.051(1) Å. Each BuTC^{4-} acts as a tetra-bidentate bridging ligand by coordinating to eight different Mn^{II} centers. The shortest interlayer distance is 3.8 Å, based on the van der Waals radii. The XRPD pattern of the $[\text{Mn}_2(\text{BuTC})(\text{DMA})_2]_n$ showed good agreement with the simulated pattern (Fig. S2†). In the TGA trace of the as-synthesized Mn-MOF in N_2 atmosphere (Fig. S3†), the two coordinating DMA molecules per formula ($[\text{Mn}_2(\text{BuTC})(\text{DMA})_2]_n$) were removed over the range 200–300 °C, and decomposition of Mn-MOF ensued above ~400 °C.

3.2. Conversion Reactions of Mn-MOF into Manganese Oxides and Their Characterization.

We explored the conversion reactions of Mn-MOF into manganese oxides. Based on the above TGA result, we first heated as-synthesized Mn-MOF under N_2 flow to 550 °C and

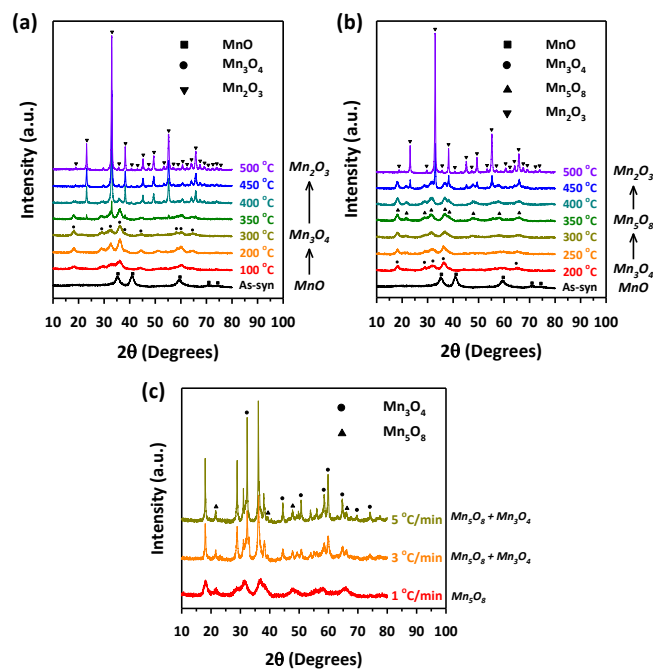


Fig. 5 Monitoring structural transformations from MnO to manganese oxides with higher oxidation numbers. XRPD patterns for MnO before and after heat treatment at various temperatures (a) in a box furnace with a ramping rate of 5 °C min^{-1} and (b) in a tube furnace under oxygen flow of 100 mL min^{-1} with a ramping rate of 1 °C min^{-1} . (c) XRPD patterns of MnO after heat treatment at 350 °C in a tube furnace under oxygen flow of 100 mL min^{-1} and with different ramping rates of 1 °C min^{-1} , 3 °C min^{-1} , and 5 °C min^{-1} .

maintained this temperature for 12 h to achieve complete thermal decomposition of the MOF structure (see the Experimental Section for details). Scanning electron microscope (SEM) images of pristine Mn-MOF and converted black powder revealed a pseudomorphic conversion process (Fig. 1). The converted material was nanoporous, as its cross-sectional SEM and TEM images (Fig. 3a and d) clearly showed the macropores and mesopores, respectively. The TEM image revealed that the frameworks of the converted material were composed of small nanoparticles of ~5 nm. A high-resolution (HR) TEM image of this material (Fig. 3d, inset) exhibited distinct lattice fringes indicating the highly crystalline nature of these nanoparticles. The XRPD pattern of the converted material identifies its structure as single-phase cubic manganosite (MnO), which is coincident with JCPDS No. 71-4748 (Fig. 4, bottom). The cubic MnO phase could be confirmed by its electron diffraction pattern (Fig. 3d, inset) as well. The crystalline size of MnO nanoparticles, calculated by applying the Scherrer equation to the (200) reflection, was 5.0 nm in diameter. The elemental analysis revealed that the nanoporous MnO contained residual carbon (18 wt%) and nitrogen (0.6 wt%).

Using the nanoporous MnO that has the lowest oxidation state among the manganese oxide structures as a precursor, we further carried out sequential conversion reactions under an oxidizing environment to generate manganese oxides with higher oxidation states. First, nanoporous MnO was heated in

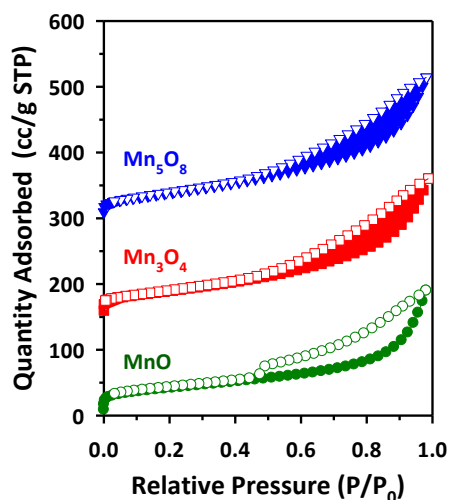


Fig. 6 Nitrogen adsorption–desorption isotherms of converted manganese oxides.

ambient air. The XRPD patterns monitored at incremental heating temperatures (Fig. 5a) indicated that the transformation of cubic MnO into a tetragonal spinel-phase hausmannite-Mn₃O₄ (JCPDS No. 24-0734, hereafter Mn₃O₄) started at 100 °C, and the latter phase was maintained up to 300 °C. At 350 °C, several new peaks started to appear in the XRPD pattern, which corresponds to bixbyite Mn₂O₃ (JCPDS No. 73-1826). Further heating to ≥450 °C yielded the pure phase of Mn₂O₃. Meanwhile, conversion reactions under a more oxidative environment allowed for the stabilization of metastable intermediate Mn₅O₈; we found that the nanoporous MnO can be transformed into a pure, layered Mn₅O₈ phase by way of Mn₃O₄ phase, when it was heated to 350 °C under oxygen flow at a very slow ramping rate of 1 °C min⁻¹ (Fig. 5b and c). The heating of MnO to the same temperature but with higher ramping rates (3 or 5 °C min⁻¹) afforded a mixture of Mn₃O₄ and Mn₅O₈ phases instead of the sequential formation of pure Mn₃O₄ and Mn₅O₈ phases (Fig. 5c). Hence, the degree of oxidation environment and the change of heating rate can adjust oxidation states and purities of the resultant manganese oxides.

Under the optimized experimental conditions based on the above experiments, we could obtain Mn₃O₄ and Mn₅O₈ in pure phases via pseudomorphic transformation of nanoporous MnO (Fig. 1). Further examination of these two manganese oxides with cross-sectional SEM and TEM images (Fig. 3b, c, e and f) revealed that the nanoporous structure of MnO was retained despite the structural transformation processes. The crystalline sizes of Mn₃O₄ and Mn₅O₈, calculated by applying the Scherrer equation to the (101) and (−201) reflections of their XRPD patterns (Fig. 4), respectively, were 5.6 nm and 5.2 nm, similar to that of MnO. The crystallinity and pure phases of nanoporous Mn₃O₄ and Mn₅O₈ were also confirmed by their HR-TEM images and electron diffraction patterns (Fig. 3e and f, insets),

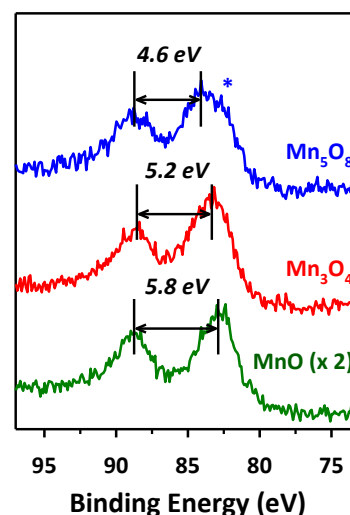


Fig. 7 Mn 3s XPS spectra of converted manganese oxides. The blue asterisk indicates the presence of low-valent (e.g. Mn²⁺) manganese species in Mn₅O₈.

respectively. However, the Mn₂O₃ showed a marked increase in the nanocrystal size, from 5.0 to ~20 nm, regardless of the reaction conditions such as the gas environment or heating rate (Fig. 5a, b and S5[†]). Hereafter, we will focus on the three phases—MnO, Mn₃O₄, and Mn₅O₈—that have almost identical textural properties, for further discussions of the converted manganese oxides.

Fig. 6 shows the nitrogen adsorption–desorption isotherms of the three manganese oxides, which feature type IV isotherms with H3-type hysteresis loops over all three samples, indicating well-developed mesoporosity. The highly porous nature of the three nanoporous manganese oxides provide similarly large Brunauer–Emmett–Teller (BET) surface areas (~145 m² g⁻¹) and pore volumes (~0.3 cm³ g⁻¹). The pore size distribution curves obtained by BJH method exhibited similar pores sizes (5 to 20 nm) of manganese oxides (Fig. S4[†]). The detailed textural data are summarized in Table S3[†]. While the N₂ adsorption data reveal similar porous properties of the three manganese oxides, the X-ray photoelectron spectroscopy (XPS) data clearly establish a marked difference in their oxidation states (Fig. 7 and Table S4[†]). The Mn 3s XPS spectra (Fig. 7) revealed that the position of the lower binding energy peak gradually shifted to higher energy with the increase in the oxidation number of the sample (MnO → Mn₃O₄ → Mn₅O₈), which is consistent with previous results.^{49–51} This systematic peak shift results in a corresponding decrease in the 3s multiplet splitting (ΔE_{3s}) of these manganese oxides (Table S4[†]).

Nanoporous manganese oxides thus far reported have been predominantly limited to those with high oxidation states such as MnO₂ and Mn₂O₃.^{9,52–58} Toward the low-oxidation-state manganese oxide, Bruce et al. prepared nanoporous Mn₃O₄ by reducing pre-synthesized nanoporous Mn₂O₃ with hydrogen gas.⁵⁸ Likewise, other nanoporous metal oxides with low

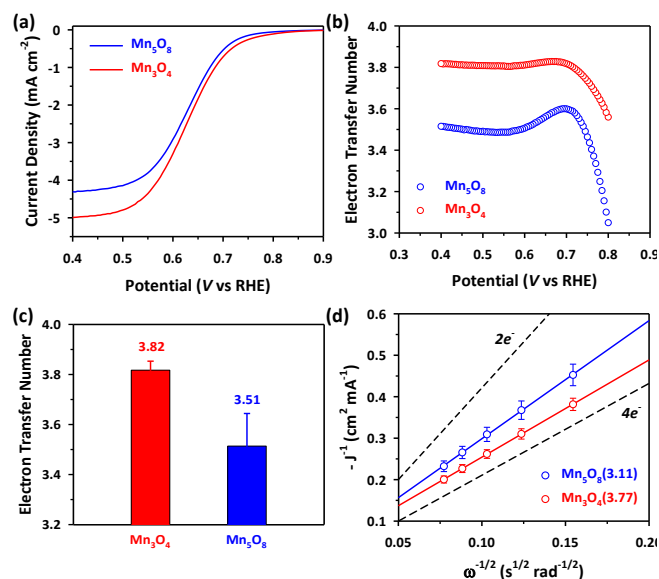


Fig. 8 Electrochemical activity of series of nanoporous manganese oxides for the ORR. (a) LSV curves of nanoporous manganese oxides on glassy carbon electrodes. (b) The numbers of electrons transferred at 0.4 V (vs. RHE) during the ORR obtained from the RRDE measurements. (c) Plot of the number of transferred electrons against potential during the ORR obtained by RRDE measurement. (d) Koutecký-Levich plots at 0.4 V (vs. RHE). The dotted lines show the theoretical slopes when two and four electrons are transferred during ORR. The numbers in the parentheses indicate the number of transferred electrons.

oxidation states, for instance, CoO and Fe₃O₄, could be prepared by the reduction of the corresponding metal oxides with higher oxidation numbers.^{59,60} In contrast, in our approach, the oxidative conversion reactions of Mn-MOF could sequentially generate nanoporous MnO, Mn₃O₄, Mn₅O₈, and Mn₂O₃, by progressively increasing the degree of oxidation. Significantly, our MOF-driven route enabled the isolation of the low-oxidation-state MnO and metastable intermediate Mn₅O₈ as pure phases with nanoporous nanocrystalline structures, which were previously rarely attainable.^{61,62} In particular, to our knowledge, nanoporous Mn₅O₈ with such a large surface area and well-developed porosity is prepared for the first time.

We note that the transformations between different structures, from cubic (MnO) to spinel (Mn₃O₄), and to layered (Mn₅O₈), occurred while preserving a nanoporous structure and textural properties. As demonstrated in our recent work,³⁰ the conversion reactions exploiting aliphatic ligand-based MOFs allow for the formation of thermally stable nanoporous metal oxide frameworks that are composed of small nanoparticles. In this approach, labile aliphatic ligands can act as self-templates during the thermal conversion process, and finally evaporate to generate nanopores. We also found that the infinite coordination between inorganic and organic moieties in the MOFs is critical for suppressing the aggregation of metallic entities into large particles; instead, the thermal conversion of a single coordination compound generated very large agglomerates.³¹ In this way, the prepared nanoporous

manganese oxide frameworks are constructed with small (~5 nm) manganese oxide nanoparticles, which have a high density of defects or grain boundaries. Compared to bulk metal oxides, nanometer scale manganese oxide nanoparticles could relieve or minimize the structural stress during the transformations between different structures, which could lead to a minimal change in their textural properties.

3.3. Electrocatalytic properties of nanoporous manganese oxides for oxygen reduction reaction.

Among the transformed nanoporous manganese oxides, Mn₃O₄ and Mn₅O₈ have nearly identical textural properties (such as morphology, surface area, and crystallite size of framework nanoparticles) and are free of residual carbon, but differ only in their oxidation states. As such, these two manganese oxides can serve as a system for the study of the oxidation state effect in catalysis. We investigated the electrocatalytic properties of the two nanoporous manganese oxides for the ORR (Fig. 8, S6†, and S7†), because the latter is a key reaction in energy conversion devices such as fuel cells and metal–air batteries. The LSV curves for the two nanoporous manganese oxides (Fig. 8a), measured in 0.1 M KOH electrolyte at a rotating speed of 1600 rpm revealed that the nanoporous Mn₃O₄ had higher on-set potential (0.75 V vs. RHE) and current density at 0.75 V (-0.26 mA cm⁻²) than those of Mn₅O₈ (0.73 V and -0.15 mA cm⁻², respectively). In addition, nanoporous Mn₃O₄ showed a higher limiting current density than Mn₅O₈. We note that nanoporous MnO showed higher current density than the other oxides in the kinetic-diffusion controlled region of the LSV curve (Fig. S8†). This result does not correspond to the previous report where MnO exhibited inferior ORR activity to Mn₃O₄.⁶³ We attribute this higher activity of the nanoporous MnO to the presence of residual carbon and nitrogen. The kinetic parameters of the two catalysts for the ORR were deduced by measurement of the ring currents during the ORR (Fig. 8b and c) and the Koutecký-Levich analyses (Fig. 8d and S6†). Results from both the methods consistently indicated that the electron numbers transferred by the nanoporous Mn₃O₄ were higher (3.8) than Mn₅O₈ (3.1–3.5). The excellent kinetics observed for nanoporous Mn₃O₄ could also be confirmed with its smaller charge transfer resistance at 0.7 V in EIS data (Fig. S7†).

Collectively, nanoporous Mn₃O₄ had higher diffusion-limited current, electron transfer number, and lower charge transfer resistance than those of Mn₅O₈. For the ORR in alkaline electrolyte, the most efficient way is direct four electron transfer mechanism, which is, however, kinetically impeded due to its high activation barrier. Instead, two-step mechanism is favored, wherein oxygen is first reduced via two electron pathway producing peroxide species (HO₂⁻) and the catalytic decomposition of HO₂⁻ produces half of oxygen molecule that is further reduced. Importantly, rapidly repeated the latter cycles lead to quasi-four-electron transfer mechanism. Comparing the oxidation state of the two manganese oxides, spinel Mn₃O₄ structure consists of Mn cations with +2 and +3

oxidation numbers, whereas layered Mn_5O_8 has +2 and +4 oxidation states. The decomposition of HO_2^- can be facilitated by facile redox mechanism between +2 and +3 Mn cations on the surface of Mn_3O_4 structure.⁶⁴ Such enhanced HO_2^- decomposition results in quasi-four-electron transfer with nanoporous Mn_3O_4 . It is suggested that the disparity in framework structure between Mn_3O_4 and Mn_5O_8 could also contribute to the difference in their ORR activity. Layered Mn_5O_8 is constructed with dense frameworks, which can impede facile adsorption of oxygen molecules. In contrast, spinel Mn_3O_4 with relatively opened framework is favorable for oxygen adsorption, thus expediting catalytic cycles. Likewise, a recent study revealed that among a series of calcium manganese oxides, $\text{Ca}_2\text{Mn}_3\text{O}_8$ that has analogous crystal structure to Mn_5O_8 thus exhibited lowest ORR activity.⁶⁵

4. Conclusions

In summary, conversion reactions using Mn-MOF precursor yielded a series of nanoporous manganese oxide structures via sequential transformations. Significantly, this transformative route allowed for the preparation of low-oxidation-state (MnO) and metastable intermediate (Mn_5O_8) phases while having nanoporous architecture, which were otherwise difficult to synthesize. Additionally, this method enabled facile structural transformations between different manganese oxide structures while preserving their structural properties. In comparative investigation of the electrocatalytic activity of nanoporous manganese oxides, Mn_3O_4 showed better ORR activity and kinetics than nanoporous Mn_5O_8 , demonstrating an important role of oxidation state for enhanced performance for the ORR.

Together with our recent work,³⁰ conversion reactions exploiting aliphatic ligand-based MOFs have been demonstrated as a versatile route to nanoporous metal oxides with nanocrystalline frameworks. This work, in particular, has shown that this transformative route can enable the preparation of nanoporous architectures with unexplored compositions. We envisage that further investigations into the MOF-driven conversion reactions can enrich the composition, structure, and function of nanoporous metal oxide materials.

Acknowledgements

This work was supported by the Korea CCS R&D Center (KCRC) grant funded by the Korean Ministry of Science, ICT & Future Planning (NRF-2013M1A8A1039968). J.H.L. and Y.J.S. acknowledge the Global PhD Fellowship (NRF-2013H1A2A1033501 and NRF-2013H1A2A1032644, respectively).

Notes and references

^a Department of Chemistry, Ulsan National Institute of Science and Technology (UNIST), 50 UNIST-gil, Ulsan 689-798, Republic of Korea. E-mail: hoirimoon@unist.ac.kr

^b School of Energy and Chemical Engineering and KIER-UNIST Advanced Center for Energy, Ulsan National Institute of Science and

Technology (UNIST), 50 UNIST-gil, Ulsan 689-798, Republic of Korea. Fax: 82-52-217-2509; Tel: 82 52 217 2522; E-mail: shjoo@unist.ac.kr

† Electronic Supplementary Information (ESI) available: X-ray crystallographic data, XRPD pattern and TGA data for Mn-MOF, pore size distribution of the nanoporous MnO, Mn_3O_4 , and Mn_5O_8 , characterization data for Mn_2O_3 , LSV polarization curves of the nanoporous manganese oxides at different rotating speeds, Nyquist plots of the nanoporous manganese oxides, and LSV polarization curves of the nanoporous manganese oxides including MnO. See DOI: 10.1039/b000000x/

‡ These authors contributed equally to this work.

1. F. Schüth, *Chem. Mater.*, **2001**, *13*, 3184-3195.
2. G. J. A. A. Soler-Illia, C. Sanchez, B. Lebeau, J. Patarin, *Chem. Rev.*, **2002**, *102*, 4093-4138.
3. H. Yang, D. Zhao, *J. Mater. Chem.*, **2005**, *15*, 1217-1231.
4. Y. Ren, Z. Ma, P. G. Bruce, *Chem. Soc. Rev.*, **2012**, *41*, 4909-4927.
5. D. Gu, F. Schüth, *Chem. Soc. Rev.*, **2013**, *43*, 313-344
6. Q. Huo, D. I. Margolese, U. Ciesla, P. Feng, T. E. Gier, P. Sieger, R. Leon, P. M. Petroff, F. Schüth, G. D. Stucky, *Nature*, **1994**, *368*, 317-321.
7. D. M. Antonelli, J. Y. Ying, *Angew. Chem., Int. Ed.*, **1995**, *34*, 2014-2017.
8. P. Yang, D. Zhao, D. I. Margolese, B. F. Chmelka, G. D. Stucky, *Nature*, **1998**, *396*, 152-155.
9. D. Grosso, C. Boissière, B. Smarsly, T. Brezesinski, N. Pinna, P. A. Albouy, H. Amenitsch, M. Antonietti, C. Sanchez, *Nat. Mater.*, **2004**, *3*, 787-792.
10. B. Tian, X. Liu, H. Yang, S. Xie, C. Yu, B. Tu, D. Zhao, *Adv. Mater.*, **2003**, *15*, 1370-1374.
11. S. C. Laha, R. Ryoo, *Chem. Commun.*, **2003**, 2138-2139.
12. J. Lee, M. C. Orilall, S. C. Warren, M. Kamperman, F. J. DiSalvo, U. Wiesner, *Nat. Mater.*, **2008**, *7*, 222-228.
13. A. Corma, P. Atienzar, H. Garcia, J.-Y. Chane-Ching, *Nat. Mater.*, **2004**, *3*, 394-397.
14. R. Buonsanti, T. E. Pick, N. Krins, T. J. Richardson, B. A. Helms, D. J. Milliron, *Nano Lett.*, **2012**, *12*, 3872-3877.
15. Y. Vasquez, A. E. Henkes, J. C. Bauer, R. E. Schaak, *J. Solid State Chem.*, **2008**, *181*, 1509-1523.
16. M. Kim, V. N. Phan, K. Lee, *CrystEngComm*, **2012**, *14*, 7535-7548.
17. B. J. Beberwyck, Y. Surendranath, A. P. Alivisatos, *J. Phys. Chem. C*, **2013**, *117*, 19759-19770.
18. W. Wang, M. Dahl, Y. Yin, *Chem. Mater.*, **2013**, *25*, 1179-1189
19. J. H. Han, S. Lee, J. Cheon, *Chem. Soc. Rev.*, **2013**, *42*, 2581-2591.
20. Y. Yin, R. M. Rioux, C. K. Erdonmez, S. Hughes, G. A. Somorjai, A. P. Alivisatos, *Science*, **2004**, *304*, 711-714.
21. Y. Sun, Y. Xia, *Science*, **2002**, *298*, 2176-2179.
22. B. Liu, H. Shioyama, T. Akita, Q. Xu, *J. Am. Chem. Soc.*, **2008**, *130*, 5390-5391.
23. S. J. Yang, C. R. Park, *Adv. Mater.*, **2012**, *24*, 4010-4013.
24. M. Hu, J. Reboul, S. Furukawa, N. L. Torad, Q. M. Ji, P. Srinivasu, K. Ariga, S. Kitagawa, Y. Yamauchi, *J. Am. Chem. Soc.*, **2012**, *134*, 2864-2867.
25. W. Cho, S. Park, M. Oh, *Chem. Commun.*, **2011**, *47*, 4138-4140.
26. X. Xu, R. Cao, S. Jeong, J. Cho, *Nano Lett.*, **2012**, *12*, 4988-4991.
27. L. Zhang, H. B. Wu, S. Madhavi, H. H. Hng, X. W. Lou, *J. Am. Chem. Soc.*, **2012**, *134*, 17388-17391.
28. M. Hu, A. A. Belik, M. Imura, Y. Yamauchi, *J. Am. Chem. Soc.*, **2013**, *135*, 384-391.
29. A. S. Hall, A. Kondo, K. Maeda, T. E. Mallouk, *J. Am. Chem. Soc.*, **2013**, *135*, 16276-16279.
30. T. K. Kim, K. J. Lee, J. Y. Cheon, J. H. Lee, S. H. Joo, H. R. Moon, *J. Am. Chem. Soc.*, **2013**, *135*, 8940-8946.
31. L. Guo, H. Arafune, N. Teramae, *Langmuir*, **2013**, *29*, 4404-4412.

32. A. H. Reidies, Manganese Compounds. In *Ullmann's Encyclopedia of Industrial Chemistry*, 6 ed.; Wiley-VCH: Weinheim, 2002; Vol. 20, pp 543-564.
33. H. Wang, L.-F. Cui, Y. Yang, H. S. Casalongue, J. T. Robinson, Y. Liang, Y. Cui, H. Dai, *J. Am. Chem. Soc.*, **2010**, *132*, 13978-13980.
34. J.-S. Lee, G. S. Park, H. I. Lee, S. T. Kim, R. Cao, M. Liu, J. Cho, *Nano Lett.*, **2011**, *11*, 5362-5366.
35. W. Wei, X. Cui, W. Chen, D. G. Ivey, *Chem. Soc. Rev.*, **2011**, *40*, 1697-1721.
36. F. Jiao, H. Frei, *Chem. Commun.*, **2010**, *46*, 2920-2922.
37. L. Mao, T. Sotomura, K. Nakatsu, N. Koshiba, D. Zhang, T. Ohsaka, *J. Electrochem. Soc.*, **2002**, *149*, A504-A507.
38. L. Mao, D. Zhang, T. Sotomura, K. Nakatsu, N. Koshiba, T. Ohsaka, *Electrochim. Acta*, **2003**, *48*, 1015-1021.
39. F. H. B. Lima, M. L. Calegario, E. A. Ticianelli, *J. Electroanal. Chem.*, **2006**, *590*, 152-160.
40. F. H. B. Lima, M. L. Calegario, E. A. Ticianelli, *Electrochim. Acta*, **2007**, *52*, 3732-3738.
41. A. J. Arvai, C. Nielsen, *ADSC Quantum-210 ADX Program*, Area Detector System Corporation; Poway, CA, USA, 1983.
42. Z. Otwinowski, W. Minor, *Methods in Enzymology*, Part A. In *Macromolecular Crystallography*; Carter Jr., C. W., Sweet, R. M., Eds.; Academic Press: New York, **1997**; Vol. 276, pp 307-326.
43. G. M. Sheldrick, *SHELXTL-PLUS*, Crystal Structure Analysis Package; Bruker Analytical X-Ray; Madison, WI, USA, **1997**.
44. J. Suntivich, H. A. Gasteiger, N. Yabuuchi, Y. Shao-Horn, *J. Electrochem. Soc.*, **2010**, *157*, B1263-B1268.
45. Z.-W. Liu, F. Peng, H.-J. Wang, H. Yu, W.-X. Zheng, J. Yang, *Angew. Chem., Int. Ed.*, **2011**, *50*, 3257-3261.
46. W. Yang, T.-P. Fellingner, M. Antonietti, *J. Am. Chem. Soc.*, **2011**, *133*, 206-209.
47. S. Wang, D. Yu, L. Dai, *J. Am. Chem. Soc.*, **2011**, *133*, 5182-5185.
48. Crystal data for $\text{Mn}_2\text{C}_{16}\text{N}_2\text{O}_{10}\text{H}_{24}$, $M_r = 514.25$, triclinic, space group *P*-1 (no. 2), $a = 6.473(13)$, $b = 7.970(16)$, $c = 10.577(2)$ Å, $\alpha = 101.69(3)^\circ$, $\beta = 102.84(3)^\circ$, $\gamma = 105.70(3)^\circ$, $V = 491.7(17)$ Å³, $Z = 1$, $d_{\text{calcd}} = 1.737$ g cm⁻³, $T = 100(2)$ K, crystal size 0.2 x 0.2 x 0.1 mm³, $\lambda = 0.69999$ Å, $2\theta = 67.92$, 136 parameters, $R_1 = 0.0379$ ($I > 2\sigma(I)$, 2865 reflections), $wR_2 = 0.1082$ (all data, 5533 reflections), GOF = 1.093. Crystallographic data are summarized in the Supporting Information.
49. M. Oku, K. Hirokawa, S. Ikeda, *J. Electron Spectrosc. Relat. Phenom.*, **1975**, *7*, 465-473.
50. V. Di Castro, G. Polzonetti, *J. Electron Spectrosc. Relat. Phenom.*, **1989**, *48*, 117-123.
51. T. Gao, P. Norby, F. Krumeich, H. Okamoto, R. Nesper, H. Fjellvag, *J. Phys. Chem. C*, **2010**, *114*, 922-928.
52. Z.-R. Tian, W. Tong, J.-Y. Wang, N.-G. Duan, V. V. Krishnan, S. L. Suib, *Science*, **1997**, *276*, 926-930.
53. A.-S. Malik, M. J. Duncan, P. G. Bruce, *J. Mater. Chem.*, **2003**, *13*, 2123-2126.
54. A. K. Sinha, K. Suzuki, M. Takahara, H. Azuma, T. Nonaka, K. Fukumoto, *Angew. Chem., Int. Ed.*, **2007**, *46*, 2891-2894.
55. M. Imperor-Clerc, D. Bazin, M. D. Appay, P. Beaunier, A. Davidson, *Chem. Mater.*, **2004**, *16*, 1813-1821.
56. J.-Y. Luo, J.-J. Zhang, Y.-Y. Xia, *Chem. Mater.*, **2006**, *18*, 5618-5623.
57. F. Jiao, P. G. Bruce, *Adv. Mater.*, **2007**, *19*, 657-660.
58. F. Jiao, A. Harrison, A. H. Hill, P. G. Bruce, *Adv. Mater.*, **2007**, *19*, 4063-4066.
59. F. Jiao, J.-C. Jumas, M. Womes, A. V. Chadwick, A. Harrison, P. G. Bruce, *J. Am. Chem. Soc.*, **2006**, *128*, 12905-12909.
60. H. Tüysüz, Y. Liu, C. Weidenthaler, F. Schüth, *J. Am. Chem. Soc.*, **2008**, *130*, 14108-14110.
61. G.-L. Xu, Y.-F. Xu, J.-C. Fang, F. Fu, H. Sun, L. Huang, S. Yang, S.-G. Sun, *ACS Appl. Mater. Interfaces*, **2013**, *5*, 6316-6323.
62. S. S. T. Bastos, J. J. M. Orfao, M. M. A. Freitas, M. F. R. Pereira, J. L. Figueiredo, *Appl. Catal., B*, **2009**, *93*, 30-37.
63. Y. Gorlin, C.-J. Chung, D. Nordlund, B. M. Clemens, T. F. Jaramillo, *ACS Catal.*, **2012**, *2*, 2687-2694.
64. T. Rhadfi, J.-Y. Piquemal, L. Sicard, F. Herbst, E. Briot, M. Benedetti, A. Atlamsani, *Appl. Catal. A.*, **2010**, *386*, 132-139.
65. X. Han, T. Zhang, J. Du, F. Cheng, J. Chen, *Chem. Sci.* **2013**, *4*, 368-376.